

## Large eddy simulation of wind loads on a long-span spatial lattice roof

Chao Li<sup>1,2\*</sup>, Q.S. Li<sup>2\*</sup>, S.H. Huang<sup>3</sup>, J.Y. Fu<sup>4</sup> and Y.Q. Xiao<sup>1</sup>

<sup>1</sup>Shenzhen Graduate School, Harbin Institute of Technology, Shenzhen 518055, China

<sup>2</sup>Department of Building and Construction, City University of Hong Kong, Hong Kong

<sup>3</sup>School of Engineering Science, University of Science and Technology of China, Hefei, 230026, China

<sup>4</sup>Department of Civil Engineering, Guangzhou University, Guangzhou 510632, China

(Received December 10, 2008, Accepted September 21, 2009)

**Abstract.** The 486m-long roof of Shenzhen Citizens Centre is one of the world's longest spatial lattice roof structures. A comprehensive numerical study of wind effects on the long-span structure is presented in this paper. The discretizing and synthesizing of random flow generation technique (DSRFG) recently proposed by two of the authors (Huang and Li 2008) was adopted to produce a spatially correlated turbulent inflow field for the simulation study. The distributions and characteristics of wind loads on the roof were numerically evaluated by Computational Fluid Dynamics (CFD) methods, in which Large Eddy Simulation (LES) and Reynolds Averaged Navier-Stokes Equations (RANS) Model were employed. The main objective of this study is to explore a useful approach for estimations of wind effects on complex curved roof by CFD techniques. In parallel with the numerical investigation, simultaneous pressure measurements on the entire roof were made in a boundary layer wind tunnel to determine mean, fluctuating and peak pressure coefficient distributions, and spectra, spatial correlation coefficients and probability characteristics of pressure fluctuations. Numerical results were then compared with these experimentally determined data for validating the numerical methods. The comparative study demonstrated that the LES integrated with the DSRFG technique could provide satisfactory prediction of wind effects on the long-span roof with complex shape, especially on separation zones along leading eaves where the worst negative wind-induced pressures commonly occur. The recommended LES and inflow turbulence generation technique as well as associated numerical treatments are useful for structural engineers to assess wind effects on a long-span roof at its design stage.

**Keywords:** long-span roof; computational fluid dynamics (CFD); large eddy simulation; wind effect; wind tunnel test.

---

### 1. Introduction

In recent years, more and more long-span structures have been built with increasing span. These long-span roof structures usually have the characteristics of light mass, high flexibility, slight damping and low natural frequencies. As the span increases, the natural frequencies generally decrease, and the susceptibility of the roof to resonant excitation by turbulent wind action increases. Therefore, wind effects on these long-span structures have some significant differences in

---

\* Corresponding Author, E-mail: [bcqsl@cityu.edu.hk](mailto:bcqsl@cityu.edu.hk) (Q.S. Li), [lichao82@gmail.com](mailto:lichao82@gmail.com) (Chao Li)

comparison with those on the roofs of smaller low-rise buildings. Holmes (2001) indicated that the quasi-steady approach, although appropriate for small buildings, is not applicable for large roofs and resonant effects may be significant. In fact, the wind-resistant design criteria of extra-long-span roof structures is not fully covered by any current code or standard in the world, although wind loads are commonly the dominant forces for such structures.

At present, there are mainly two approaches to estimate the design wind loads on buildings and structures: wind tunnel test and numerical simulation on the basis of Computational Fluid Dynamics (CFD) techniques. Numerical simulations are economic and convenient for parameter analysis, which usually are able to provide comprehensive information or results. With revolutionary increase in computer power in the last two decades, Computational Wind Engineering (CWE) as a branch of CFD has been developed rapidly to evaluate the interaction between wind and structures. The turbulence modeling techniques of CFD, such as Large Eddy Simulation (LES), Reynolds Averaged Navier-Stokes Equations (RANS) Model etc., have been widely used to predict wind flows around bluff bodies in wind engineering. The time-depending variables in RANS are decomposed into mean term and fluctuating term by Reynolds time-averaged treatment, and the resultant additive Reynolds-stress term which is regarded as energy transported through turbulence fluctuation is unresolved but modeled. The function of turbulence models is bridging a relationship between the time-averaged terms with Reynolds-stress term. Obviously, only the averaged flow variables, i.e., mean wind loads, could be obtained through RANS models (Wilcox 1993; Mochida, *et al.* 2002). Nevertheless, extensive studies such as Fu, *et al.* (2006) and Robertson, *et al.* (2007) showed that wind-induced peak pressures on long-span roofs are more than 3 times larger than associated mean pressures. Consequently, estimation of fluctuating wind loading is of importance and necessity for vibration analysis and cladding design of long-span roofs.

Attempts to predict wind effects on bluff bodies using unsteady RANS equations, even with today's most advanced turbulence model, have been made with limited success (Huang, *et al.* 2007). As demonstrated by Cheng, *et al.* (2003), Kim (2004), Zhang, *et al.* (2006) and others, LES is an effective tool for simulation of unsteady flows around bluff bodies. However, as commented by Murakami (1998), there are four difficulties in applying LES for wind engineering: (1) inflow boundary condition; (2) outflow boundary condition; (3) grid stretching; (4) near wall treatment. The last three difficulties can be minimized or overcome with usage of super high-performance computers and parallel processing techniques. The convective boundary condition can be used for a more accurate description of outflow. The numerical errors induced by too big grid sizes and stretch ratio could be reduced if expensive grids systems are adopted. Wall functions are economical and helpful in dealing with near-wall turbulence. Since the generation of inflow turbulent flow field satisfying the characteristics of atmospheric boundary layer wind is always a very important issue for LES (Tutar and Celik 2007), much attention and effort should be devoted to this topic.

In this paper, an effective inflow turbulence generation approach, which was recently developed by two of the authors (Huang and Li 2008) based on the discretizing and synthesizing random flow generation (DSRFG) technique, is adopted. The validity of LES integrated with the DSRFG technique, their effectiveness and accuracy to predict the distributions and characteristics of wind-induced pressures on an extra long-span spatial lattice roof (Shenzhen Citizens Centre) will be assessed on the basis of wind tunnel test results. The 486m-long roof of Shenzhen Citizens Centre is one of the longest spatial lattice roof structures in the world, which is an ideal structure to examine the capability of CFD techniques for evaluation of wind effects on complex long-span roofs. Since the boundary layer wind tunnel has been the basic tool of wind engineering research on wind effects

on buildings and structures, it would be quite useful to conduct a wind tunnel test to provide valuable information on wind effects on the long-span roof for validation of the CFD techniques. In parallel with the numerical investigation, simultaneous pressure measurements on the entire roof of Shenzhen Citizens Centre were made in a boundary layer wind tunnel to determine wind loads on the roof.

This paper presents a combined numerical simulation and wind tunnel study of wind effects on the extra-long-span roof of Shenzhen Citizens Centre, which mainly contains three parts. The first part introduces the wind tunnel experiment arrangements. Then, the distributions and characteristics of wind-induced pressures on the roof are numerically predicted by LES integrated with DSRFG. Finally, a detailed comparative study based on the comprehensive numerical results and the model test data is presented to explore a useful approach for evaluation of wind effects on a complex curved roof using CFD techniques.

## 2. Wind tunnel experiment

Wind tunnel experiment for Shenzhen Citizens Centre was carried out in a boundary layer wind tunnel with a working section of  $3\text{m} \times 2\text{m} \times 20\text{m}$  (width $\times$ height $\times$ length). A rigid model with a geometric length scale of 1: 400 was made to represent the Shenzhen Citizens Centre. Fig. 1 shows a photo of the model mounted in the wind tunnel. Spires and roughness elements were used to simulate a typical boundary layer wind flow specified in the Chinese Load Code (2001) as exposure C category. This city terrain type specifies a mean wind speed profile with a power law exponent of  $\alpha=0.22$  and a gradient height of 1 m in the model test (400 m in full-scale), which satisfies the equation below:

$$U = \begin{cases} U_{ref}(z/z_{ref})^{0.22} & 0 < z \leq 1\text{m} \\ U_{grad} & z \geq 1\text{m} \end{cases}, \quad (1)$$

where the wind speed  $U_{ref}$  at the reference height ( $z_{ref}=0.6\text{m}$ ) was 7.5 m/s in the experiment. The spectrum of longitudinal wind speed at the height of 90 m in full-scale (0.225 m above the wind



Fig. 1 Model of the SZCC in the wind tunnel test

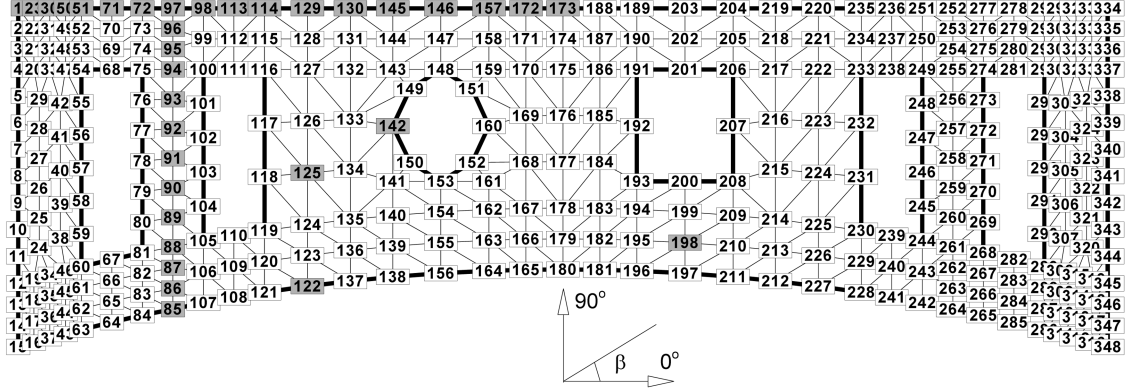


Fig. 2 Layout and serial number of the pressure taps on both upper and lower roof surfaces

tunnel test section) was found to agree with the von Karman type spectrum well. The expression of the von Karman type spectrum is

$$S_u(f) = \frac{4(I\bar{U})^2 \frac{L}{U}}{\left[1 + 70.8 \left(\frac{fL}{U}\right)^2\right]^{5/6}}, \quad (2)$$

where  $I$  is the turbulence intensity.

Both the upper and lower surfaces of the roof of Shenzhen Citizens Centre are exposed to wind flows. Therefore, in order to obtain the pressure differences between both sides of the roof, 348 pairs of pressure taps were installed at the same locations on both the upper and lower roof surfaces for the pressure measurements. The layout and serial number of the pressure taps on both the upper and lower roof surfaces are shown in Fig. 2. In the wind tunnel test, pressures were measured simultaneously from all the taps on both the roof surfaces, and data sampling frequency was 312.5 Hz and sampling length was 20480. Incident wind direction was defined as an angle  $\beta$  from the east along anti-clockwise direction, as shown in Fig. 2 and  $\beta$  varied from  $0^\circ$  to  $360^\circ$  with incremental step of  $15^\circ$  for the pressure measurements.

The pressure coefficient at tap  $i$  on the roof surface is defined as follows:

$$C_{p_i}(t) = \frac{p_i(t) - p_\infty}{p_0 - p_\infty}, \quad (3)$$

where  $p_i(t)$  is the measured surface pressure at the tap  $i$ ;  $p_0$  and  $p_\infty$  are the total pressure and the static pressure at the reference height, respectively. The detailed information about the wind tunnel test can be found in Fu and Li (2007). Selected model test data will be presented in this paper mainly for comparison with the numerical results.

### 3. Numerical modeling

Shenzhen Citizens Centre (SZCC), as shown in Fig. 1, is located in the central district of

Shenzhen City, China. It has about 210,000 square meters gross building area. The roof consists of three parts: one central part and two symmetric wings. The roof of the SZCC is a spatial lattice structure supported by tree-shaped steel columns and two towers underneath. The two towers are located in the central part: one is a twelve-story circular-shaped tower with a 36 m diameter; the other is a fifteen-story rectangular-shaped tower with a plan area of  $36 \text{ m} \times 45 \text{ m}$ . The roof is 486 m long, and its width changes from 120 m in the central part to 154 m at its two ends, while its depth varies from 2.25 m to 9.00 m. The height from ground to the top of the roof is 80 m. The upper and lower surfaces of the roof are all curve shaped. The two symmetric wings have a double-layer tetrahedral spatial lattice structure with bolt-connected ball joints, supported by 17 tree-shaped columns.

In this study, the commercial CFD software Fluent 6.2 together with the DSRFG technique recently proposed by two of the authors (Huang and Li 2008) for generation of inflow turbulent flow field were used to simulate the three-dimensional (3D) flow-field around the SZCC and wind-induced pressures on the roof. Fluent is based on the Finite Volume Method (FVM) which starts simulation with discretizing the computational domain into some small volumes. The detailed computational treatments and algorithms will be addressed in the following sections.

### 3.1. Computational domains and grids arrangements

In order to compare the results of the CFD simulations with those of the wind tunnel test, the computational model of the SZCC is established in the same scale as the wind tunnel test. As shown in Fig. 3, the maximum size of the SZCC computational model in longitudinal (X) direction, lateral (Y) direction and vertical (Z) direction is 0.385 m, 1.215 m and 0.2 m respectively. To eliminate the influences of outer boundaries and ensure achieving the fully-developed turbulence conditions, the dimensions of the computational domain were set to be  $8.5 \text{ m}(X) \times 4.0 \text{ m}(Y) \times 1.0 \text{ m}(Z)$ .

Because the elevation of the roof varies from 30 m to 70 m in full scale, in which the turbulence intensity of the atmospheric boundary layer (ABL) is relatively high and velocity changes dramatically, an accurate simulation of the wind flow profile near ground is essential. In order to obtain the desired profile of incident wind flow and avoid discretization errors introduced by tetrahedral grids, we employed hexahedral grids which can simulate shear flow of ABL well in the upstream flow-field. In addition, the roughness effects of ground have also been taken into account. As depicted in Fig. 3, the geometry of the SZCC is so complicated that the whole domain is difficult to be filled with utter hexahedral grids, and so it was decided to generate a boundary-layer mesh attached to the roof surfaces. As shown in Figs. 4 (a) and (b), hybrid mesh type called “Hex Core” (Fluent. Inc. 2006) was adopted in the central region of the computational domain to improve computing efficiency. “Hex

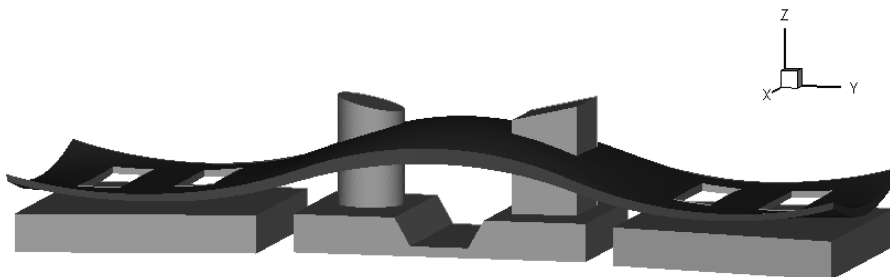


Fig. 3 Computational model of the SZCC

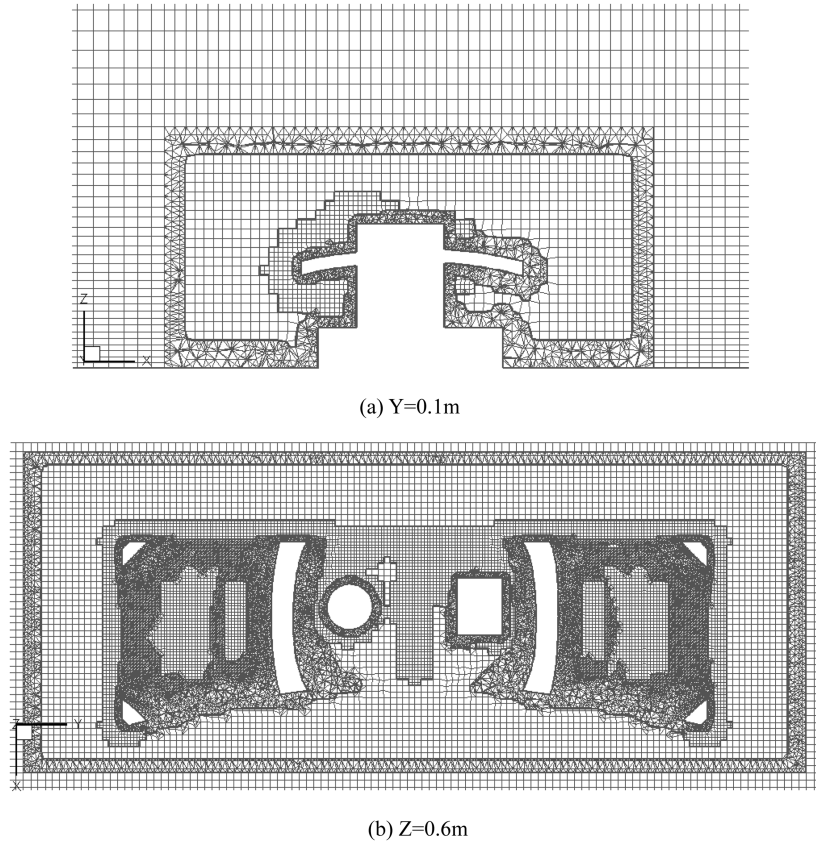


Fig. 4 Hybrid grids system for the case of 90° wind angle

Core” mesh fits the complicated building geometries using the tetrahedral grids which are more flexible and the “core” of the computational domain with the hexahedral grids which are more convergent. The minimum grid length is 0.004 m, while the maximum grid length is 0.02 m, and the grid stretching ratio is kept to be no larger than 1.05 in the whole domain for reducing the difference of cut-off wave number between neighboring grids in LES (Huang, *et al.* 2007). For the computational model subjected to incident wind angle of 90° shown in Fig. 4, the total number of cells is 1,631,533. When the “Hex Core” grid is applied in the central region of the computational domain for the computational model under wind action with incident direction of 45°, the quality of cell skewness will become rather worse, so only the tetrahedral grids are used in this case and the total cell number is increased to 2,276,948 which is about 1.5 times more than the computational model with incident wind angle of 90°. Furthermore, grid dependency tests are carried out for both wind angles. In the tests, we change the minimum grid length to 0.002 m, and the corresponding cell number is about 3 millions using Hex Core grid. The comparisons of the grid dependency test results are discussed in 4.1.

### 3.2. Large eddy simulation

As it is well known, turbulent flows are characterized by eddies with a wide range of length and time scales. Since the large eddies are more problem-dependent and anisotropic, whereas the small

eddies are less dependent on boundary and tend to be more isotropic, their extremely distinct characters imply that resolving the large and small eddies respectively is quite applicable. In Fluent (Kim 2004), grid spacing is used as a filter function in LES to separate turbulence into large eddies and small eddies. The large ones are resolved directly through the governing equations whereas the influences of small ones are taken into account by a modeling approach, which is known as sub-grid scale (SGS) model. Apparently, LES is less computational resources consuming than Direct Numerical Simulation (DNS) for the modeling of small eddies, but retains the unsteady large-scale coherent structures and is hence compatible with a wider range of turbulent flow than RANS. These advanced features make LES more appropriate for evaluation of unsteady complex ABL flows around and wind effects on buildings and structures.

Until now, the pursuit of a universal SGS model, which bears partial responsibility for obstructing the practical application of LES, has never ceased. The original SGS model, Smagorinsky (S) model proposed by Smagorinsky (1963), has been widely used since the pioneering work of Deardorff (1970). To correct the drawback of  $C_s$ , which is a constant used for defining the SGS viscosity  $M_s$ , several improved SGS models have been proposed. The well-known dynamic Smagorinsky model (DS) is the most successful one which was proposed by Germano, *et al.* (1991) and revised by Lilly (1992). However, the underlying assumption adopted both in the S model and the DS model is that the local equilibrium exists between the transferred energy through the grid-filter scale and the dissipation of kinetic energy at small sub-grid scales. The dynamic SGS kinetic energy (DKE) model (Kim and Menon 1995) describes the SGS turbulence by accounting for the transport of the SGS turbulence kinetic energy, which was found to be better than an algebraic expression based on local equilibrium assumptions given by the Smagorinsky series. In fact, for high Reynolds number bluff body flows, the local equilibrium assumption is questionable. Therefore, the dynamic SGS kinetic energy model is employed in this study.

For the purposes of comparison and also for determination of the initial flow-field, one of the RANS models, RNG  $k-\varepsilon$  is also used in this study.

### 3.3. Numerical algorithms

Wind flow motion that is concerned in wind engineering applications is relatively slow and can be considered as incompressible flow in general. The segregated approach was selected for solving of the discretized continuity and momentum equations and a second order implicit formulation was used for the temporal discretization. The Semi Implicit Method for Pressure Linked Equation Consistent (SIMPLEC) scheme, part of the Semi Implicit Method for Pressure Linked Equation (SIMPLE) family of algorithms, was used for solving the pressure-velocity coupling. For unsteady state problems, SIMPLEC converges faster than SIMPLE and is more stable than Pressure-Implicit with Splitting of Operators (PISO) scheme when the computational time-step is relatively small in LES (Fluent, Inc. 2007). The skewness correction technique was also introduced to reduce convergence difficulties associated with highly distorted tetrahedral meshes. The Bounded Central Differencing (BCD) Scheme, which is a composite of a pure central differencing, a blended scheme of the central differencing and the second-order upwind scheme, and the first-order upwind scheme, was used for the spatial discretization of momentum and sub-grid kinetic energy. Apparently, a comparatively accurate prediction of flow field as the initial condition will lead the iterative calculations to converge more quickly and reduce the time needed for LES to reach a statistically stable mode, so an initial velocity field was generated based on the steady state results of the RNG  $k-\varepsilon$  model.

### 3.4. Boundary conditions

#### 3.4.1. Inflow turbulence generation method

The inflow turbulence generation method, namely DSRFG recently proposed by two of the authors (Huang and Li 2008), which can produce a fluctuating velocity field satisfying any given spectrum including the von Karman spectrum, is adopted in this study. According to the DSRFG method, an isotropic fluctuating velocity field in  $\mathbf{x}$  space can be synthesized by the following superposition of harmonic functions:

$$u_i(\mathbf{x}, t) = \sum_{n=1}^N [\mathbf{v}(k_j^n) \cos(k_j^n x_j + \omega_n t) + \mathbf{w}(k_j^n) \sin(k_j^n x_j + \omega_n t)] \quad (4)$$

$$\mathbf{v}(\mathbf{k}_n) = \boldsymbol{\zeta}_n \times \mathbf{k}_n, \quad \mathbf{w}(\mathbf{k}_n) = \boldsymbol{\xi}_n \times \mathbf{k}_n \quad (5)$$

$$\boldsymbol{\zeta}_i^n, \boldsymbol{\xi}_i^n \in N(0, 1), \quad \omega_n \in N(0, \omega_0), \quad (6)$$

where  $\mathbf{x}$  and  $t$  are vector of space coordinates and time, respectively;  $\omega_0$  is a positive number dependent on the correlation of fluctuating velocity, and  $N(M, \sigma)$  represents a normal distribution with mean of  $M$  and standard deviation of  $\sigma$ . For 3D problems, when the limit  $N \rightarrow \infty$  and  $\mathbf{k}_n$  is isotropically distributed on the surface of a sphere of radius  $k_0$ , the resulting velocity field satisfies

the spectrum  $E(k) = \frac{3}{2} u_{rms,i}^2 \delta(k - k_0)$ . Noting that the spectrum  $E(k)$  has a non-zero value at and

only at  $k_0$ , which is a very flexible feature that can be utilized in the construction of a spectrum with arbitrary shape.

The DSRFG method produces an inflow fluctuating velocity field using a procedure of discretization and synthesis. The detailed derivation of the DSRFG method is given by Huang and Li (2008) and a simple formulation of the method is presented below.

$$\mathbf{u}(\mathbf{x}, t) = \sum_{m=k_0}^{k_{max}} \mathbf{u}_m(\mathbf{x}, t) = \sum_{m=k_0}^{k_{max}} \sum_{n=1}^N [\mathbf{p}^{m,n} \cos(\tilde{\mathbf{k}}^{m,n} \cdot \tilde{\mathbf{x}} + \omega_{m,n} t) + \mathbf{q}^{m,n} \sin(\tilde{\mathbf{k}}^{m,n} \cdot \tilde{\mathbf{x}} + \omega_{m,n} t)], \quad (7)$$

where  $\mathbf{p}^{m,n} = \frac{\boldsymbol{\zeta} \times \mathbf{k}^{m,n}}{|\boldsymbol{\zeta} \times \mathbf{k}^{m,n}|} \sqrt{\alpha \frac{4E(k_m)}{N}}$ ,  $\mathbf{q}^{m,n} = \frac{\boldsymbol{\xi} \times \mathbf{k}^{m,n}}{|\boldsymbol{\xi} \times \mathbf{k}^{m,n}|} \sqrt{(1-\alpha) \frac{4E(k_m)}{N}}$ ,  $\tilde{\mathbf{x}} = \frac{\mathbf{x}}{L_s}$ ,  $\tilde{\mathbf{k}}^{m,n} = \frac{\mathbf{k}^{m,n}}{k_0}$ ,  $|\mathbf{k}^{m,n}| = k_m$ ,  $\omega_{m,n} \in N(0, 2\pi f_m)$ ,  $f_m = k_m U_{avg}$ .  $\boldsymbol{\zeta}_i^n$  and  $\boldsymbol{\xi}_i^n$  are defined as the same as those given in Eq. (6).  $k_m$  is wave number.  $L_s$  is turbulence integral length scale which is an important parameter used as the scaling factor for spatial correlation.  $\alpha$  is a random number uniformly distributed between 0~1.  $N=100$  (sampling number for each wave number  $k_m$ ) and sampling frequency  $f_{max}=500$  are found to be accurate enough and economical for the present research.

The DSRFG method was programmed and parallelized as a User-Defined-Functions library in Fluent code. The DSRFG method can generate an inflow field satisfying target profiles of velocity and turbulence intensity as well as make longitudinal fluctuating velocity spectrum be consistent with those in the wind tunnel test. Turbulence integral length scale represents the correlation

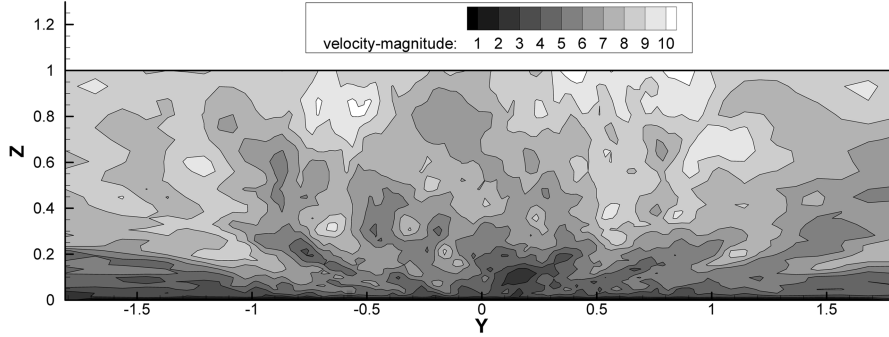


Fig. 5 A instantaneous inflow velocity contour map generated at  $t=4.2s$

characteristics of large scale turbulence vortices. However, in wind tunnel tests, it is hard to simulate the variation of the turbulence scale with height in proportion to that observed in the ABL (Li and Melbourne 1999; Li, *et al.* 2000, 2003, 2004). For this reason, a semi-empirical formula for determination of turbulence integral scale stipulated in “AIJ Recommendations for Loads on Buildings” (AIJ 2004) is adopted in the present numerical simulations. After a reduced scale transformation, it has the form:

$$L_s = \begin{cases} 0.25 \times (z/0.075)^{0.5} & z > 0.075 \\ 0.25 & z \leq 0.075 \end{cases} \quad (8)$$

An instantaneous velocity contour map generated at  $t=4.2s$  is plotted in Fig. 5.

### 3.4.2. Near-wall flow treatments

Unlike wind flows in regions somewhat far from walls, both the mean velocity field and the turbulence in near-wall regions are significantly affected by the presence of walls. Consequently, it is rather critical that the flows in a near-wall region should be calculated with great caution. The computation of near-wall flow motions by LES requires a mesh satisfying  $y^+ \approx 1$ , where  $y^+ \approx \rho y u_\tau / \mu$ ,  $y$  is the normal distance from the wall at cell centers,  $u_\tau$  is the friction velocity which is determined by  $u_\tau = \sqrt{\tau_w / \rho}$ ,  $\tau_w$  is the wall shear stress,  $\rho$  is the air density,  $\mu$  is the dynamic viscosity. However, the complex flow motions such as impinging and boundary layer separation etc. around buildings make  $y^+$  change rapidly along the wall. For instance,  $y^+$  of the final mesh in this study takes values approximately from 1 to 100. So an “Enhanced Wall Function” is employed to formulate the law-of-the-wall as a single wall law for the entire wall region (Fluent, Inc. 2007). Enhanced Wall Function can be regarded as a compromise of the two traditional near-wall treatments (i.e., the standard wall function proposed by Launder and Spalding (1974) and the near-wall modeling approach), which is therefore chosen for LES in this study for the sake of considering its advantages of economy, reasonably accuracy and general applicability for bluff body flow simulations.

A similar approach, called “Enhanced Wall Treatment”, which calculates the near-wall region flows by a two-layer model method when the centroid of the first layer grids falls in laminar sub-layer, is chosen for the RNG  $k-\varepsilon$  simulation.

### 3.4.3. Other boundary conditions

Based on the assumption that the wind flows are fully-developed at outlet, an outflow condition that combines a zero diffusion flux for all flow variables in the direction normal to the exit plane with an overall mass balance correction is imposed.

The side faces and upper boundary of the computational domain are imposed free-slip boundary conditions where the normal velocity components and the normal gradients of all velocity components are assumed to be zero. The free-slip boundary conditions are realized by modifying the shear stress of wall condition equaling to zero.

### 3.5. Post processing

Time-step size for the present LES was set as 0.001s, which is small enough to capture the phenomena such as random velocity fluctuations and periodic vortex shedding. Thus, the corresponding sampling frequency should be taken to be 1000 Hz. However, due to the restriction of our computer capability, the sample length  $N$  was taken to be 4000 in the LES, which is shorter than that in the wind tunnel test.

The along-wind length of the computational domain was 8.5m, while the wind speed at the eave height of the SZCC model mounted at the frontal 1/3 position of the domain was 5.89 m/s. Therefore, after the ABL inflow was imposed at inlet for two seconds, the flow-field was considered as statistically stable enough for sampling data. All the data for statistical post-processing were collected from the beginning of the third second to the end of the sixth second. The simulations were run on a Linux cluster including 16 nodes. A complete DSRFG-LES simulation process for the present grid system took about 5 days with 20 processes. A DSRFG-LES computation requires about 15% time longer than a normal LES simulation.

The tree-shaped steel columns that support the roof were not considered in the present computational models. Comparison of the LES simulated pressure values on the lower roof with those from the wind tunnel test revealed noticeable discrepancies between the two sets of results, which implied that these columns may have remarkable influences on the computed pressure distributions on the lower roof. So only the computed pressures on the upper roof will be discussed in this paper. The time-series of pressures at 348 locations on the upper roof, at the same tap locations as the wind tunnel test, were obtained by the LES. Although the present LES can provide much more information than the wind tunnel test, only the simulation results at the 348 tap locations are presented and discussed below for the purposes of comparison with the wind tunnel test data.

The identical data analysis methods were used for analyzing both the numerical simulation results and wind tunnel test data. The pressure coefficient at the tap  $i$  is determined by the following formula:

$$C_{pi} = \frac{p_i(t)}{\frac{1}{2} \times \rho V_{ref}^2}. \quad (9)$$

It is noted that, in a wind tunnel test, the dynamic pressure, as expressed in Eq. (3), could be calculated by the subtraction of the total pressure and static pressure. The total pressure is measured in the front of a model at a given reference height, and the static pressure is measured outside the flow field, sometimes inside a scaled building model where is totally static without wind velocity. In

Fluent, the numerator of Eq. (9) is called gauge pressure. For incompressible flows that do not involve any pressure boundaries, Fluent solver will let the gauge pressure field subtract the pressure in the cell located at (or nearest to) the “reference pressure location” after each iteration to ensure the gauge pressure at the reference pressure location is always zero. It is no doubt that the fluctuation of pressure at the reference pressure location could influence the whole gauge pressure field, so finding a location in the computational domain where the pressure can be kept from fluctuating is significant. On the other hand, we do not have such a problem in the wind tunnel test because the “reference location” is usually positioned outside the flow field, where the pressure can be regarded as absolutely static. In the present simulation, we imposed an inflow with very low turbulence intensity on the first few mesh layers near the top slip boundary, and the reference pressure location was in a cell right above the building model near the top boundary. The effects of the pressure fluctuation at the reference location will be revealed in Section 4.4. Equations for evaluation of mean, root-mean-square (rms), peak pressure coefficients, skewness and kurtosis of pressure coefficients, peak body type variation, and correlation coefficients will be presented as follows:

$$\text{Mean pressure coefficient: } C_{pi,mean} = \sum_{n=1}^N C_{pi}/N \quad (10)$$

$$\text{Fluctuating pressure coefficient: } C_{pi,rms} = \sqrt{\sum_{n=1}^N (C_{pi} - \bar{C}_{pi})^2 / (N-1)} \quad (11)$$

$$\text{Pressure coefficient skewness: } C_{pi,sk} = \sum_{n=1}^N (C_{pi} - \bar{C}_{pi})^3 / N / C_{pi,rms}^3 \quad (12)$$

$$\text{Pressure coefficient kurtosis: } C_{pi,ku} = \sum_{n=1}^N (C_{pi} - \bar{C}_{pi})^4 / N / C_{pi,rms}^4 \quad (13)$$

$$\text{Peak pressure coefficient: } C_{pi,peak} = \bar{C}_{pi} - g \times C_{pi,rms} \quad (14)$$

$$\text{Peak body type variation coefficient: } \mu_{si,peak} = C_{pi,peak} \left( \frac{z_{ref}}{z_i} \right)^{2\alpha} \quad (15)$$

$$\text{Fluctuating pressure correlation coefficient: } \rho_{ij} = \frac{E[(C_{pi}(t) - \bar{C}_{pi})(C_{pj}(t) - \bar{C}_{pj})]}{C_{pi,rms} C_{pj,rms}} \quad (16)$$

where  $\rho$  is the air density,  $z_i$  is the height of the tap  $i$ ,  $E$  is the expected value,  $g$  is the peak factor and its calculation will be introduced later.

## 4. Numerical results and discussions

### 4.1. Mean pressures

When the wind approaches a roof with sharp eaves, complex flow patterns such as separation and

vortex shedding may occur, and these shedding vortices either reattach on the roof or dissipate in the open wake flow. These highly turbulent vortices generally produce large suction pressures, which is the key factor resulting in damages of long-span roofs. If the streamline of incoming flow is perpendicular to the leading edge of eave, a columnar vortex will be produced behind the leading edge. If the wind flow does not approach in the direction normal to eave edge, namely a quartering wind, two counter rotating vortices (i.e., conical vortices) along two side corners on the roof could be generated (He and Song 1997; Franchini, *et al.* 2005; He, *et al.* 2007). The contours of the mean pressure coefficient on the upper roof of the SZCC for the approaching wind angles of  $90^\circ$  and  $45^\circ$ , which were obtained by the CFD simulation and the wind tunnel test, are shown in Fig. 6. For the

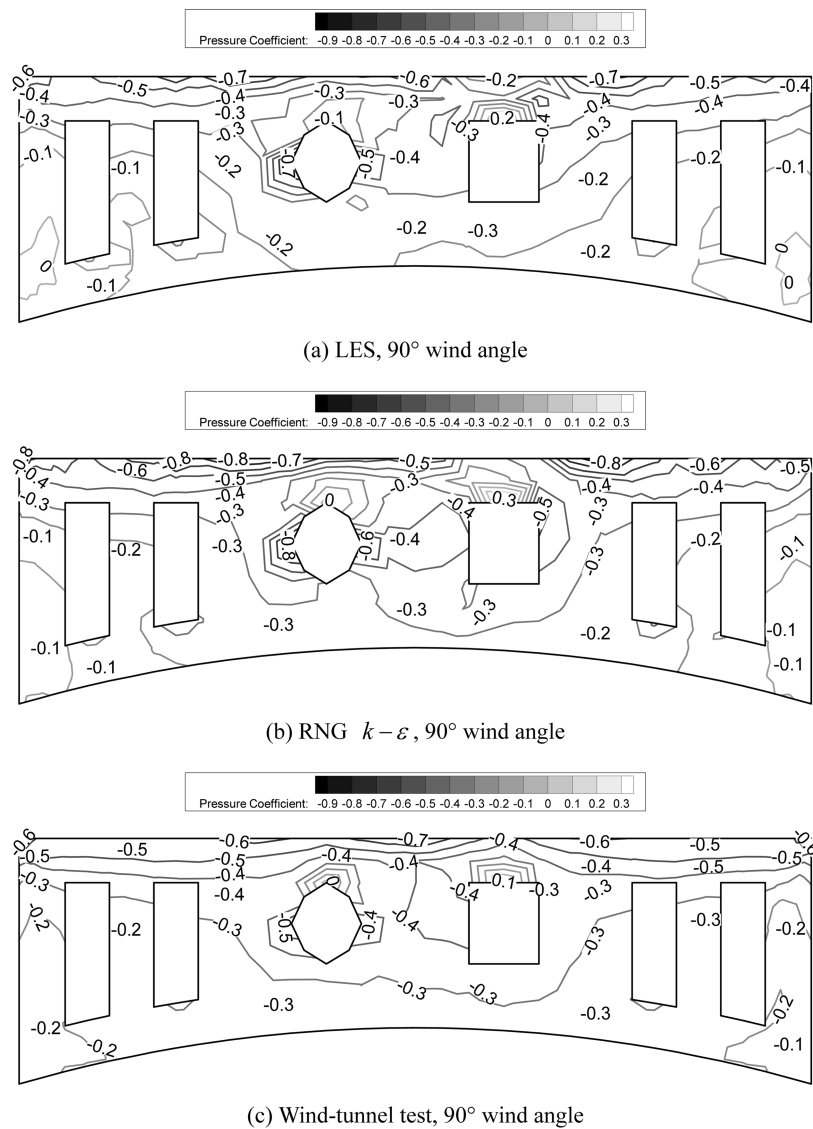
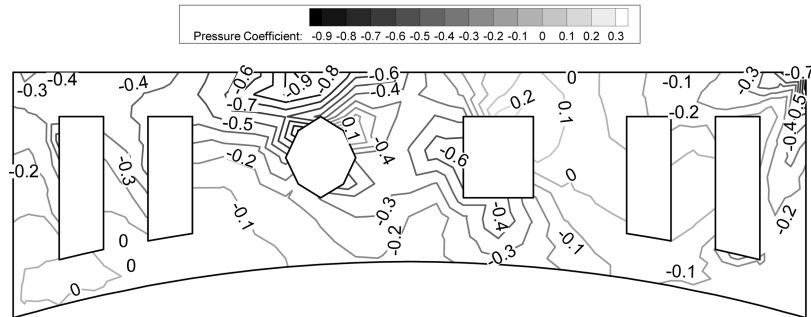
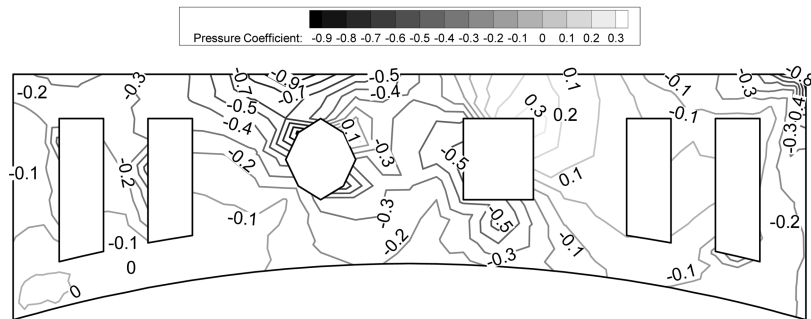


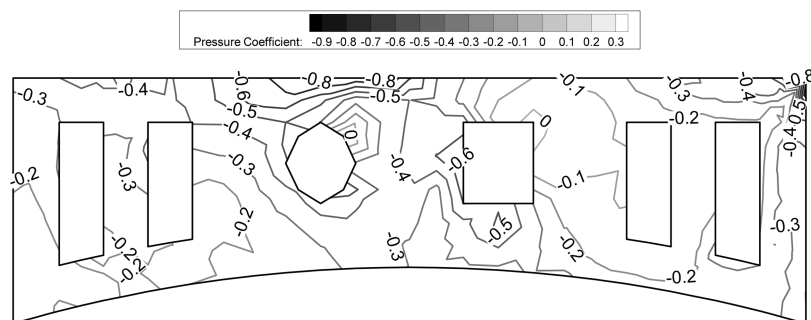
Fig. 6 Contours of the mean pressure coefficient on the upper roof



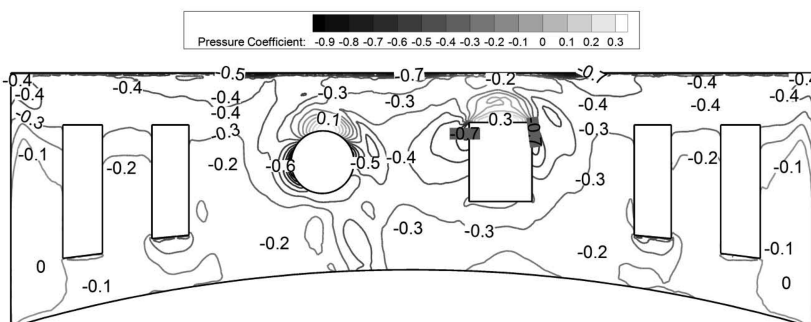
(d) LES, 45° wind angle



(e) RNG  $k-\epsilon$ , 45° wind angle



(f) Wind-tunnel test, 45° wind angle



(g) LES, 90° wind angle, generated using mesh grid points

Fig. 6 Continued

case of wind angle of  $90^\circ$ , the pressure contour lines are distributed symmetrically. It can be illustrated by these figures that the mean suction peaks occur right behind the windward eave edge, which is induced by wind flow separation at the roof corners or leading edges. In the flow re-attaching region, the magnitude of the mean suction becomes smaller.

A comparison of the difference of  $C_{p,mean}$  between the CFD and wind tunnel test results is shown in Table 1. RNG1 and LES1 represent the results corresponding to the adopted meshes using a minimum length of 0.004, and RNG2 and LES2 represent the results associated with the meshes using a minimum length of 0.002. No remarkable discrepancy of the mean pressure on the upper roof was observed between the results from the current computational model and those from a denser mesh model. The difference of the standard deviation (Std.)  $C_{p,mean}$  of between the CFD and wind tunnel test results is around 0.07 in  $90^\circ$  and 0.075 in  $45^\circ$ , respectively.

In the flow separation zone, RNG  $k-\varepsilon$  model overestimates the maximum mean suction at the roof leading edge, such as at taps 220, 130 for incident wind angle of  $90^\circ$ , and at tap 334 for  $45^\circ$ . The maximum  $C_{p,mean}$  below the wind tunnel test results (Max. under) is around -0.31. However, LES can give more reasonable prediction results in the separation zone. For incident wind angle of  $90^\circ$ , the maximum difference between the LES and the model test results is around -0.21 and occurred at tap 142 where flow separations and vortex shedding were induced by the circular tower side edge. For the case of incident wind angle of  $45^\circ$ , the associated maximum difference is around -0.26 and occurred at tap 334 near the roof leading edge.

In the flow reattaching zone, the RNG  $k-\varepsilon$  yields better results than the LES. It is understood that the roof curvature's little variation may lead to the wind-induced pressure distribution changing dramatically. It is observed that the LES and the RNG can predict positive pressures for the roof segments with a rising curve.

The obstruction effects induced by the circular and square towers (See Fig. 3) in the middle regions of the roof can also be observed from the simulated or experimental results shown in Fig. 6. As the approaching separated flows impinged on the windward faces of the towers, there are two positive pressure regions on the roof caused by the re-circulating flows. Both the LES and RNG  $k-\varepsilon$  model can predict these local positive pressures, but overestimate them. The maximum  $C_{p,mean}$  values obtained by the two CFD models, which are higher than the wind tunnel results (Max. over), are found at taps 189, 201, and 206 in this area.

When  $\beta=90^\circ$ , high magnitudes of suction occurred at taps 142 and 160 shown in Fig. 6 (a), (b) and (c), which may be attributed to the generation of the horseshoe-vortices along the circular tower

Table 1 Differences of  $C_{p,mean}$  between the CFD and wind tunnel test results

Wind angle	Differences*	RNG1		RNG2		LES1		LES2	
		Value	Tap	Value	Tap	Value	Tap	Value	Tap
$90^\circ$	Max. over	0.252	189	0.239	201	0.295	189	0.288	189
	Max. under	-0.321	220	-0.335	130	-0.215	142	-0.209	142
	Std.	0.069		0.070		0.070		0.072	
$45^\circ$	Max. over	0.357	206	0.365	206	0.284	206	0.304	206
	Max. under	-0.316	334	-0.305	334	-0.263	334	-0.258	334
	Std.	0.074		0.076		0.078		0.074	

\*Note: Max. over: the maximum difference of over-estimations by CFD; Max. under: the maximum difference of under-estimations by CFD; Std.: the standard deviation of differences between CFD and model test results.

side edge. Similarly, it was found that both the LES and RNG  $k-\varepsilon$  model could capture two local high suction on the two sides of the square tower, which are marked in grey color in Fig 6. (g). For the purpose of comparison with the experimental data, Figs. 6 (a)-(f) are plotted using the computed pressure values at the same locations with the 348 pressure taps mounted on the upper side of the roof. On the other side, to show the advantage that CFD could provide much more detailed information than the wind tunnel test, Fig. 6 (g) was generated directly using the pressure values at all the grid nodes. Apparently, the number of grid nodes on the upper roof is much more than 348. Nevertheless, in the wind tunnel test, due to limited number of pressure taps installed in this area, no distinct pressure gradient was found from Fig. 6 (c). Obviously, CFD could overcome the number restriction of pressure taps in wind tunnel tests.

#### 4.2. RMS fluctuating pressures

Fluctuating pressure coefficient (See Eq. (11)), one of the important characteristics of wind loads on roof surfaces, reflects turbulent energy magnitude of pressure fluctuation including all scales of vortices. The contour maps of fluctuating pressure coefficients obtained by the LES and the experiment are shown in Fig. 7. Compared with the contours of the mean pressure coefficients in Fig. 6, one can find the similar distribution trends in these contour lines. Both the maximum mean and fluctuating pressure coefficients are found at the windward roof corner and their absolute-values decrease gradually from the leading edge to the rear edge. Explanation for the similarity is that the rotation, attachment and rolling-up of the intermittent separated vortices are the major cause of mean and fluctuating suction. Fig. 8 illustrates the instantaneous phenomena like separation, re-attachment and vortex shedding simulated by the LES.

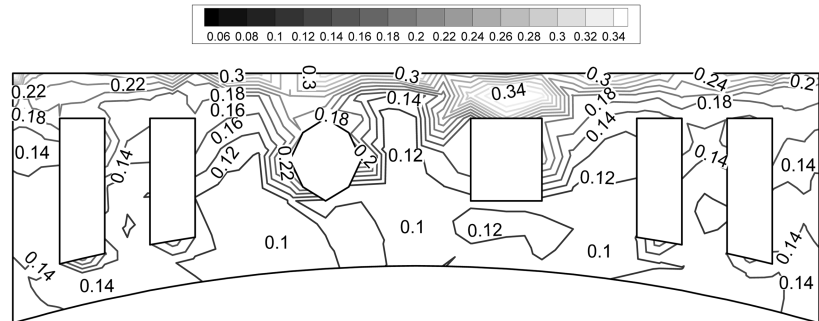
When  $\beta=90^\circ$ , Fig. 8 (b) shows the unsteady streamlines in the  $y=0.1$  m plane, which indicates that the LES has the ability to reproduce the vortex movements in the tower's upstream and downstream wind flows. As shown in Fig. 7 (a) and (b), the maximum fluctuating pressure occurs around tap 202 in the front of the square tower, while the fluctuating pressures behind the tower are much smaller.

When  $\beta=45^\circ$ , the greatest fluctuating pressure is observed at the windward roof corner where conical vortices start rolling-up along the eave, and the regions affected by the conical vortices are subjected to intensive turbulent pressures. The horseshoe-vortices induced by the square tower also lead to high fluctuation around tap 198.

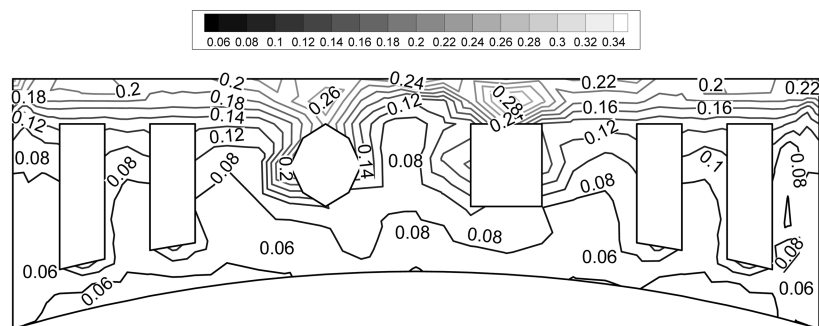
It can be summarized from the results presented in Fig. 7 that the rms pressure values simulated by the LES have approximately the same distributions with the corresponding wind tunnel test results. However, it is observed that the fluctuating pressure coefficients predicted by the LES are generally larger than the experimental data, which will be discussed in Section 4.4.

#### 4.3. Power spectra of pressure fluctuations

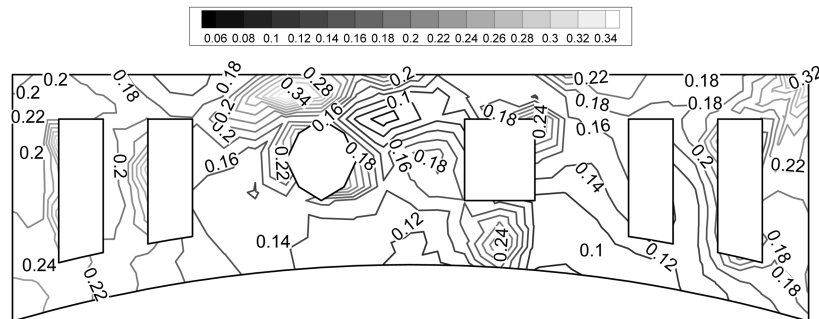
As observed by Li, *et al.* (2000, 2003, 2004), their field measured power spectral densities of fluctuating wind speed in longitudinal, lateral and vertical directions were in good agreement with the von Karman-type spectra, suggesting that the von Karman-type spectra can describe the energy distribution fairly well for the three wind velocity components over typical urban areas. The inflow spectra generated both in the wind tunnel test and the LES are plotted in Fig. 9 (a). The target von Karman spectrum is also presented for comparison purpose. It is evident that the spectra simulated by the present LES and the model test match the von Karman spectrum very well.



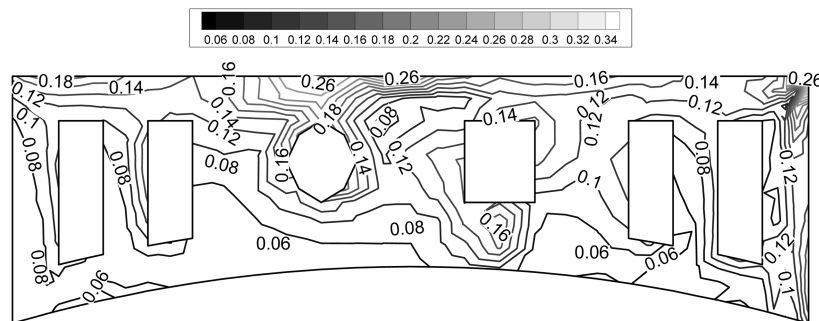
(a) LES, 90° wind angle



(b) Wind tunnel test, 90° wind angle



(c) LES, 45° wind angle



(d) Wind tunnel test, 45° wind angle

Fig. 7 RMS pressure coefficient distributions on the upper roof

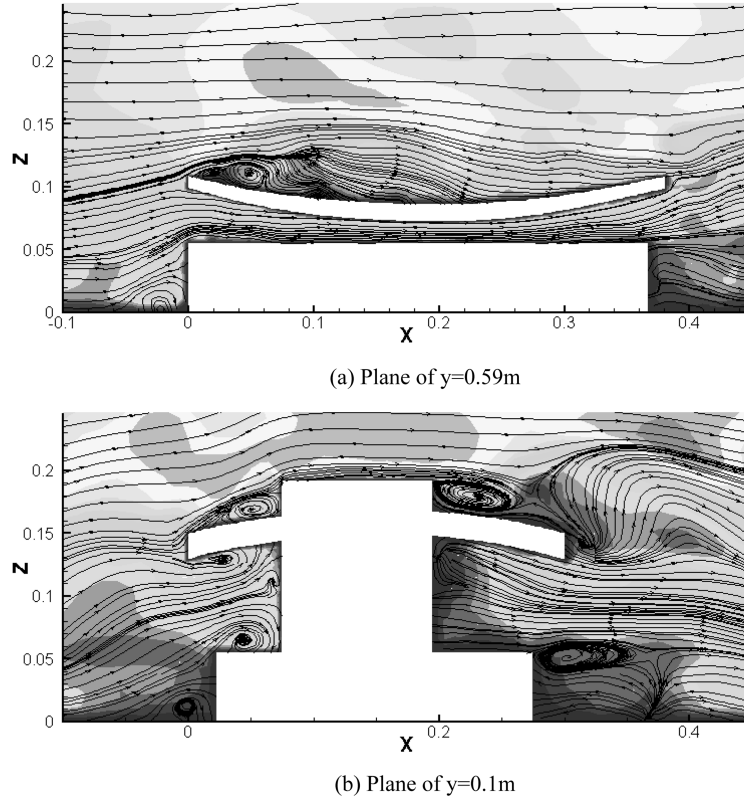


Fig. 8 Unsteady streamlines simulated by the LES

Figs. 9 (b)-(f) show the simulated and measured dimensionless pressure spectra along with transformed von Karman pressure spectra as a function of reduced frequency,  $f^*=fH/U_h$ , where  $H$  is the mean height of the building roof and  $U_h$  is the incident mean wind speed at  $H$ . Y-coordinate is

the normalized pressure spectrum,  $S_{p,i}^*(f) = \frac{fS_{p,i}(f)}{P_{ref}^2}$ , where  $S_{p,i}(f)$  is the power spectral density (PSD)

of pressure at tap  $i$ ,  $P_{ref}^2$  is the mean reference dynamic pressure squared, and the PSD was calculated using Welch's method (Welch 1967) by MATLAB code. For the reasons discussed in Section 3.5, the sampling frequency and sample size of the CFD simulations and the experiment were not identical, and the obtained minimum threshold frequency of the LES signals is 0.9435 Hz, which is acceptable for analysis of wind loading on the long-span roof.

Figs. 9 (b), (c) and (d) present the spectra of pressures measured at taps 129, 125 and 122 selected along the longitudinal direction (for the case of  $\beta=90^\circ$ ). For tap 129 located in the separation zone at windward eave, more energy is contained in lower frequency band and the PSD is almost uniformly distributed in this region. Energy decay is observed for the reduced frequencies exceeding 0.5. For tap 125 in the middle region of the roof, compared with the case at tap 129, more energy is moved from the lower frequency regions to higher bands, which implies the separated vortices are decomposed into smaller scales with the interaction between flow and the roof. For tap 122 in the rear region of the roof, the PSD curve distributes smoothly over the full frequency bands and drops

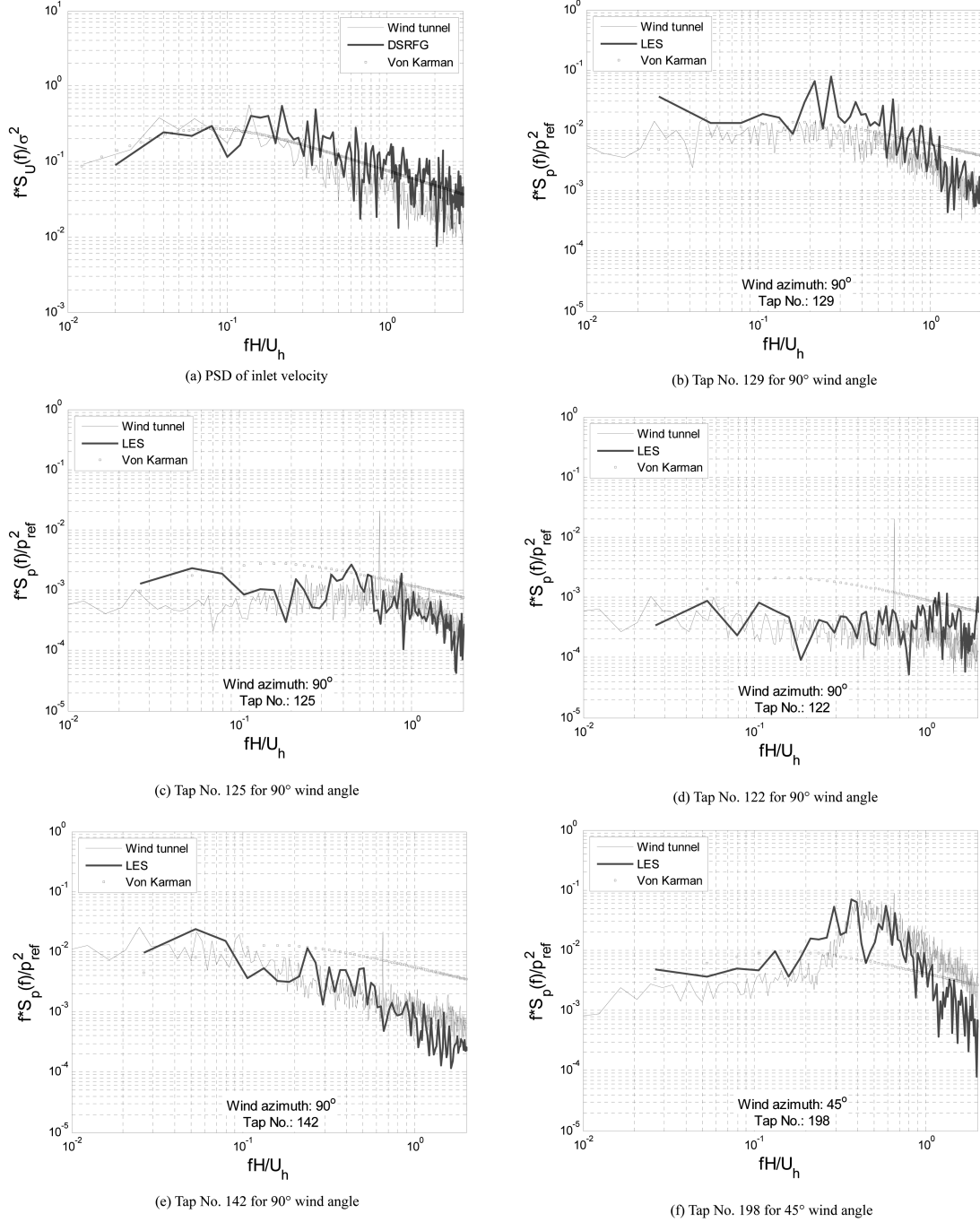


Fig. 9 Power spectral densities

down slowly as the frequency increase, indicating the structures of vortices become fully out-of-order and the ratio of each scale is uniform. Tap 142 located right near the local boundary layer separation

point where the wind flow is passing the circular tower, more fluctuating energy is distributed in the lower-frequency ranges. As shown in Fig. 8 (f), the mean reduced frequency of the horseshoe-vortices induced by the square tower near tap 198 is estimated around 0.5.

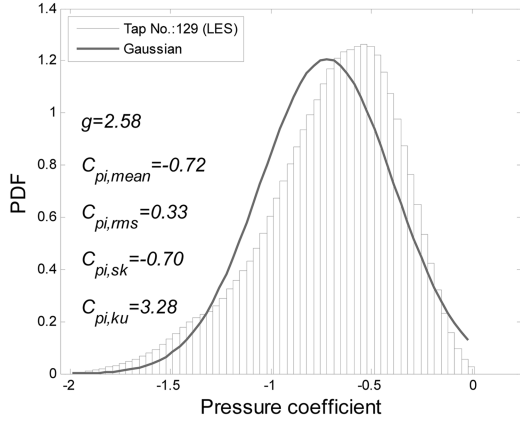
A number of previous studies have revealed that the quasi-steady theory fails to adequately predict pressures under separated flows, in particular beneath or near conical vortices (Letchford, *et al.* 1993; Uematsu and Isyumov 1998; Banks and Meroney 2001). From the comparison between the pressure and transformed von Karman pressure spectra shown in Fig. 9, obviously, we could come to a similar conclusion. These pressure fluctuations are induced by turbulent flows distinct from fully-developed ABL flows.

The combination of the DSRFG and the LES provides numerical simulations which are in good agreement with the wind tunnel test results when the power spectra of wind-pressures on the roof are concerned. The observations from the comparative study on all the measured and simulated pressure spectra are summarized as follows: (1) The spectra by the LES in the separated zone along the leading edge show a better agreement than those in the re-attaching zone. This may be due to the fact that the roof's surface curvature variations and openings, possibly, make it difficult to accurately simulate the flow development along the roof. (2) Frequency specialties of flow patterns like local boundary separation and vortex-shedding can be predicted well by the LES.

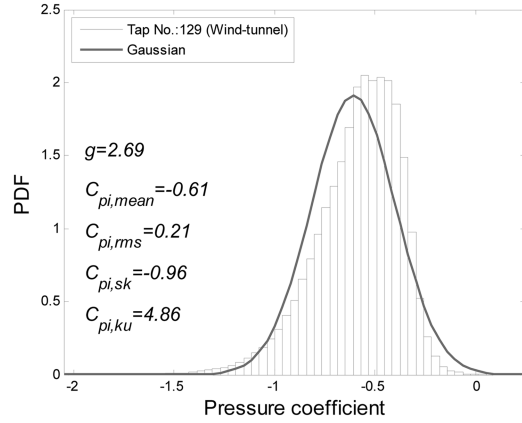
#### 4.4. Probabilistic characteristics of pressure fluctuations

Failures of most long-span roofs are induced by the chain reactions from one local claddings' destruction due to extreme wind pressure actions in a short period. In order to determine the peak values of pressures, it is of great importance to analyze the probabilistic characteristics of wind-induced pressures on roofs. The shape of a probability density function (PDF) can be characterized by its third and fourth central moments relative to the standard deviation values. The pressure coefficients skewness,  $C_{p,sk}$ , and the kurtosis,  $C_{p,ku}$ , were defined in Eqs. (12) and (13), respectively. For a normal or Gaussian distribution, skewness and kurtosis are equal to 0 and 3, respectively. Skewness is a measure of the asymmetry of the data around the sample mean.  $C_{p,sk} < 0$  corresponds to  $C_p$  spread out more to the left, while  $C_{p,sk} > 0$  to the right. Kurtosis is a measure of how outlier-prone a distribution is.  $C_{p,ku} > 3$  represents distributions more peaked than the Gaussian and  $C_{p,ku} < 3$  characterizes distributions flatter than the Gaussian.

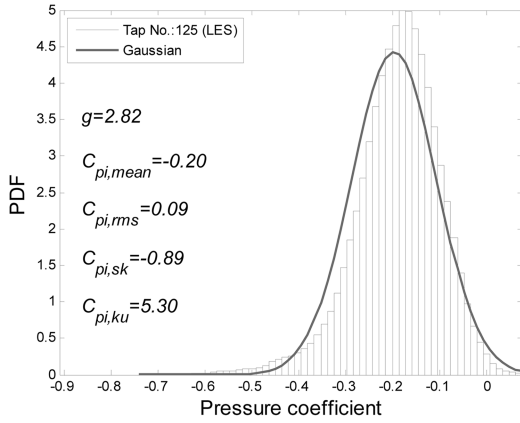
As pointed out by Li, *et al.* (1999), the distributions of wind-induced pressures in the region of flow separation were found clearly negative skewed and appeared the non-Gaussian behavior, as also noted by other researchers (Holmes 1981; Ahmad and Kumar 2002). Fig. 10 shows the mean, rms, skewness, kurtosis and probability distributions of fluctuating pressures (histograms) measured at three taps in the frontal (tap 129), middle (tap 125) and rear (tap 122) regions on the roof for incident wind angle of 90°. The full range of pressure coefficient is divided into 50 intervals for construction of the histograms. Scaled Gaussian probability density functions are also plotted in these figures for comparison purposes. For convenience of comparison, the Gaussian PDFs are scaled by multiplying the range of value and reciprocal of the number intervals 50, which makes the sum of y-axis values of histograms equal the projective area of the scaled Gaussian PDFs. It can be seen from the experimental data (See Figs. 10 (b), (d) and (f)) that with the tap position moving downstream, the skewness decreases gradually. The PDF distribution for the rear tap 122 is quite close to the Gaussian. However, all the kurtoses are larger than 3. Both the negative skewness and large kurtosis will lead to a higher probability for the large negative pressures than those predicted



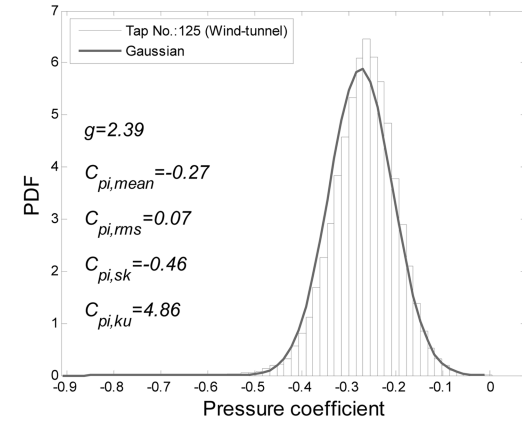
(a) Probability distribution for Tap 129 by the LES



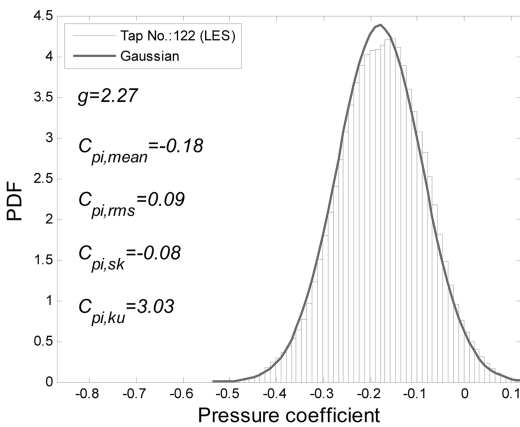
(b) Probability distribution for Tap 129 by the wind tunnel test



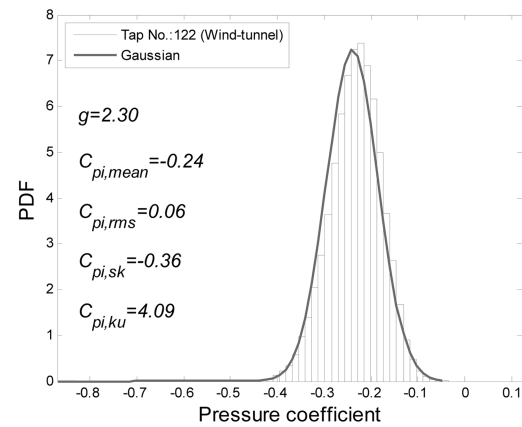
(c) Probability distribution for Tap 125 by the LES



(d) Probability distribution for Tap 125 by the wind tunnel test



(e) Probability distribution for Tap 122 by the LES



(f) Probability distribution for Tap 122 by the wind tunnel test

Fig. 10 Probability distributions of pressure coefficient

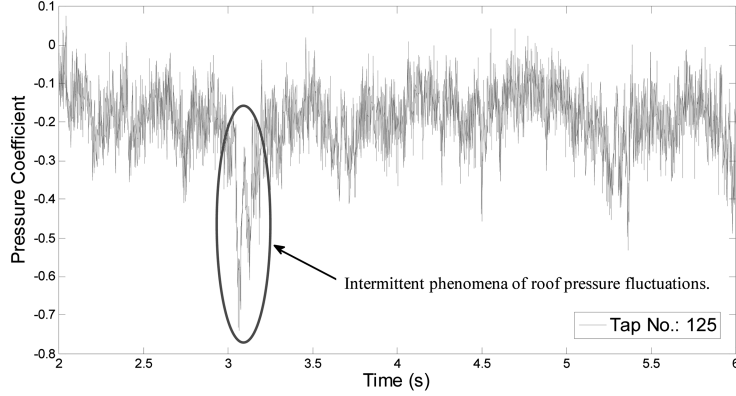


Fig. 11 Simulated wind pressure coefficient time series for tap 125

by a Gaussian PDF. The results of the LES (See Figs. 10 (a), (c) and (e)) show small deviations from those of the wind tunnel test. The kurtoses of the PDFs for taps 129 and 122 by the LES are 1.5 and 1.05 which are less than the experimental results, indicating the distributions of the LES results are flatter than the experimental ones, and this may be one of the reasons why the fluctuating pressure coefficients predicted by the LES are larger than the experimentally determined ones.

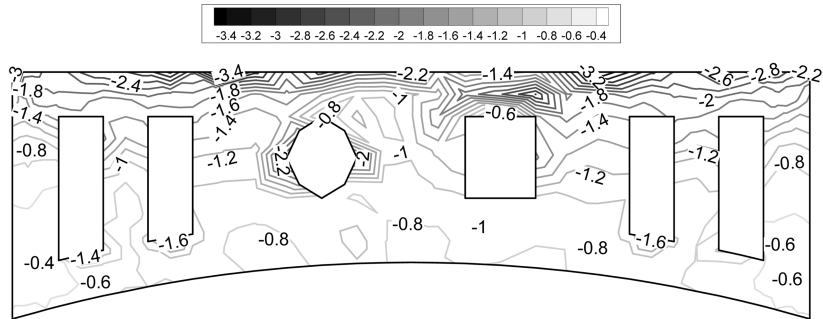
The results of  $C_{p,sk}=-0.81$  and  $C_{p,ku}=5.06$  from tap 125 have moderate deviations from the corresponding experimental data and other LES results. After analyzing the wind pressure coefficient time series, occurrence of very low pressure fluctuations was found from 3s to 3.3s, shown in Fig. 11. This phenomenon appeared in separation and reattaching flows has been observed in many field measurements and wind tunnel tests (e.g., Li and Melbourne 1999). The results plotted in Fig. 11 demonstrate that the LES is able to predict the intermittent phenomena of roof pressure fluctuations.

Based on the calculated probability distributions of wind-induced pressures, a simple probability method is used to compute the peak factor  $g$ , where  $g_i = \frac{|C_{pi,obj} - C_{pi,mean}|}{C_{pi,rms}}$ .  $C_{pi,obj}$  is the pressure coefficient

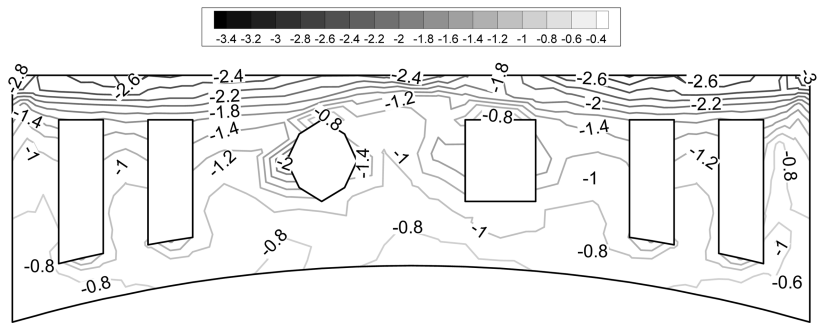
threshold corresponding to a probabilistic confidence level which is chosen as 98.5% in the present study. As a result, the pressure coefficient signals from the tap  $i$  greater than  $C_{pi,obj}$  account for 98.5 percent of total signals. The calculated peak factors at taps 129, 125 and 122 are plotted in Fig. 10. For the purpose of comparing CFD simulation results with the Chinese Loading Code (2001), peak body type variation coefficients  $\mu_{s,peak}$  were calculated for all the 348 taps using Eqs. (14) and (15), and the contour maps are plotted in Fig. 12. It is apparent that both the distributions of peak body type variation coefficients and values of peak factor agree well between the simulated and experimental results.

#### 4.5. Spatial correlation of pressure fluctuations

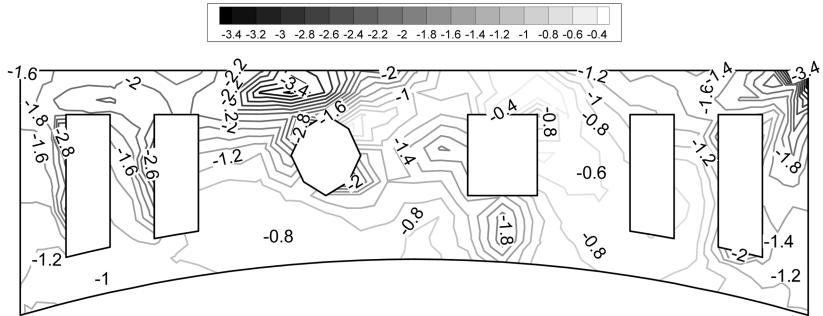
As defined in Eq. (16), spatial correlation coefficient  $\rho_{ij}$  for fluctuating pressures at two points,  $i$  and  $j$  reflects their relationships of tendencies to augment or reduce for a same instant. The structure scales and trajectories of vortices induced by the interactions between wind flows and the building



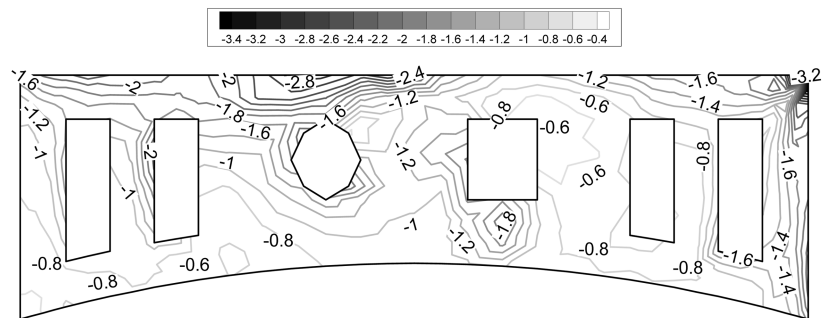
(a) LES, 90° wind angle



(b) Wind tunnel test, 90° wind angle

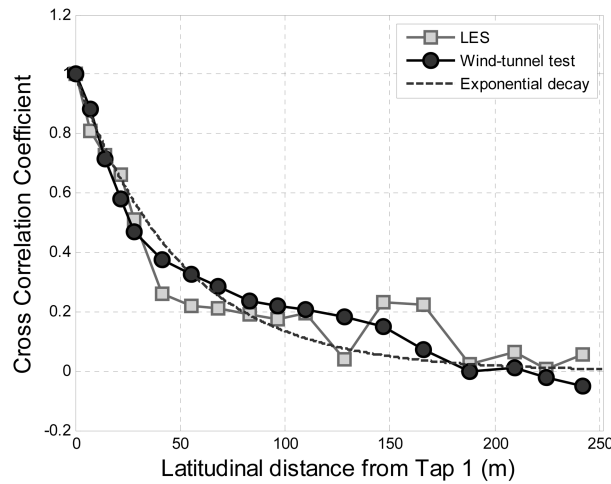


(c) LES, 45° wind angle

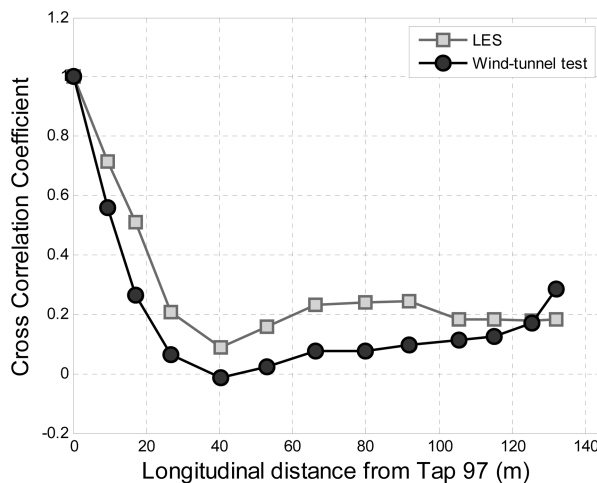


(d) Wind tunnel test, 45° wind angle

Fig. 12 Peak body type variation coefficient on the upper roof



(a) Cross correlation coefficient for a row of taps in lateral direction. From left to right, the order of tap number is 1, 23, 30, 50, 51, 71, 72, 97, 98, 113, 114, 129, 130, 145, 146, 157, 172, 173 (See Fig. 2).



(b) Cross correlation coefficient for a column of taps in longitudinal direction. From left to right, the order of tap number is 97, 96, 95, 94, 93, 92, 91, 90, 89, 88, 87, 86, 85 (See Fig. 2).

Fig. 13 Comparison of the pressure correlations by the LES and the wind-tunnel test

roof are also related with the spatial correlation coefficient.

The cross correlation coefficients between tap 1 with the other 17 taps in the first row are plotted in Fig. 13(a), where the abscissa is the full-scale distance from the first tap. As shown in Fig. 13(a), the correlation coefficient curves from the LES and the wind tunnel tests are in good agreement. The results shown in this figure also indicate that the correlations of pressure fluctuations are descending by the increase of distances from tap 1 gradually. One simple correlation function for wind velocity, which is expressed in the exponential decay formulation proposed by Davenport (1968), is also plotted by dashed line in Fig. 13(a) for comparison purposes. Since the fluctuating dynamic

pressure  $p'$  are related to fluctuating velocity  $u'$  through  $p' = C_p \rho \bar{U} u'$  under quasi-steady theory, it is not surprised to note that the correlation function of velocity in the expression of  $\rho_{ij} = \exp\left(-\frac{|y|}{50}\right)$

fits well with the correlation coefficients of roof pressure fluctuations. This coincident event may suggest that the correlation of fluctuating pressure at the taps along the leading edge is somewhat dependent on the incoming flow fluctuation, when the incident wind direction is perpendicular to the leading edge.

The correlations of wind pressures on roof surfaces are dominated by the separation, reattachment and shedding of vortices, and intensity of correlation is determined by the sizes and trajectories of separated vortices (Richards and Hoxey 2006). Several taps on the roof along the longitudinal wind direction far away from the square tower are selected to determine their pressure correlations. The computational results together with the experimental data are plotted in Fig. 13(b). The minimum correlation coefficient is found at tap 93 based on both the wind tunnel and LES results, and then it is deduced that the average reattachment position is around the location at tap 93. As mentioned in Section 3.2, in the LES the fluctuations of vortices larger than the filter size are calculated directly. However, the turbulence fluctuations smaller than filter size which may play a role in decreasing the correlation are neglected. Because the flow correlation is more dominated by the large scale turbulence, the correlations predicted by the LES are larger than the wind tunnel test results.

## 5. Conclusions

The LES technique integrated with a turbulent velocity inflow field generation method (DSRFG) was adopted in the present study to simulate the turbulent flow-field around the SZCC and the pressure distributions on the long-span roof. Based on the detailed comparative study between the numerical simulations and the wind tunnel test, conclusions are summarized as follows:

- 1) The mean pressure coefficients predicted by the LES and RNG  $k-\varepsilon$  model were found to agree well with the experimental data in general. In the separation zone, the LES can provide quite reasonable results compared with the experimental results. In the reattached zone, the RNG  $k-\varepsilon$  yields relatively better results.
- 2) The magnitudes of fluctuating pressure coefficients simulated by the LES are slightly larger than the experimental results. Moreover, the LES is able to capture the intermittent phenomena of pressure fluctuations on the roof.
- 3) For most pressure taps, the PSD of fluctuating pressure in separation zone at the eave edge match the experimental results well, and there are fairly small deviations between the numerical predictions and measured results for the taps located in the reattaching regions. It is impressive that the non-Gaussian characteristics of pressure fluctuations in separation zones can be effectively simulated by the present LES.
- 4) The spatial correlations of wind-induced pressures on the roof in the longitudinal and lateral wind directions simulated by the present LES were found to be in good agreement with the wind tunnel test results, revealing that the vortex structures induced by the interaction between wind flow and the roof could be predicted well by the LES.

In summary, the present LES integrated with the DSRFG technique could provide satisfactory predictions of wind effects on the long-span roof with complex shape. It is encouraging to obtain the

simulation results comparable with the wind tunnel measurements. It is thus concluded that the recommended LES and inflow turbulence generation techniques as well as associated numerical treatments are useful for structural engineers to assess wind effects on a long-span roof at its design stage.

## Acknowledgement

The work described in this paper was fully supported by a grant from City University of Hong Kong (Project No. 7002315), which is gratefully acknowledged. The authors are thankful to the reviewers for their useful comments and suggestions.

## References

- Ahmad, S. and Kumar, K. (2002), "Effect of geometry on wind pressures on low-rise hip roof buildings", *J. Wind Eng. Ind. Aerod.*, **90**(7), 755-779.
- Architectural Institute of Japan (2004), *Recommendations for loads on buildings*.
- Banks, D. and Meroney, R.N. (2001), "The applicability of quasi-steady theory to pressure statistics beneath rooftop vortices", *J. Wind Eng. Ind. Aerod.*, **89**(6), 569-598.
- Cheng, Y., Lien, F.S., Yee, E. and Sinclair, R. (2003), "A comparison of large eddy simulations with a standard k-epsilon Reynolds-averaged Navier-Stokes model for the prediction of a fully developed turbulent flow over a matrix of cubes", *J. Wind Eng. Ind. Aerod.*, **91**(11), 1301-1328.
- Davenport, A.G. (1968), "The dependence of wind load upon meteorological parameters", *Proc. of the Int. Research Seminar on Wind Effects on Buildings and Structures*, University of Toronto Press, Toronto, 19-82.
- Deardorff, J.W. (1970), "A numerical study of three-dimensional turbulent channel flow at large Reynolds numbers", *J. Fluid Mech.*, **41**, 453-480.
- Fluent, Inc. (2007), *Fluent 6.3 User's Guide*.
- Fluent, Inc. (2006), *Gambit 2.3 Documentation*.
- Franchini, S., Pindado, S., Meseguer, J. and Sanz-Andres, A. (2005), "A parametric, experimental analysis of conical vortices on curved roofs of low-rise buildings", *J. Wind Eng. Ind. Aerod.*, **93**(8), 639-650.
- Fu, J.Y., Li, Q.S. and Xie, Z.N. (2006), "Prediction of wind loads on a large flat roof using fuzzy neural networks", *Eng. Struct.*, **28**(1), 153-161.
- Fu, J.Y. and Li, Q.S. (2007), "Wind effects on the World's longest spatial lattice structure: loading characteristics and numerical prediction", *J. Constr. Steel Res.*, **63**, 1341-1350.
- GB50009-2001 (2002), *Load code for the design of building structures*, Beijing: China Architecture & Building Press.
- Germano, M., Piomelli, U., Moin, P. and Cabot, W.H. (1991), "A dynamic subgrid-scale eddy viscosity model", *Phys. Fluids*, **3**, 1760.
- He, H., Ruan, D., Mehta, K.C., Gilliam, X. and Wu, F. (2007), "Nonparametric independent component analysis for detecting pressure fluctuation induced by roof corner vortex", *J. Wind Eng. Ind. Aerod.*, **95**(6), 429-443.
- He, J. and Song, C.C. (1997), "A numerical study of wind flow around the TTU building and the roof corner vortex", *J. Wind Eng. Ind. Aerod.*, **67-68**, 547-558.
- Holmes, J.D. (1981), "Non-Gaussian characteristics of wind pressure fluctuations", *J. Wind Eng. Ind. Aerod.*, **17**, 103-108.
- Holmes, J.D. (2001), *Wind Loading of Structures*, Spon Press.
- Huang, S.H. and Li, Q.S. (2008), "A general inflow turbulence generator for large eddy simulation", submitted to *J. Wind Eng. Ind. Aerod.*
- Huang, S.H., Li, Q.S. and Xu, S. (2007), "Numerical evaluation of wind effects on a tall steel building by CFD", *J. Constr. Steel Res.*, **63**(5), 612-627.
- Kim, S. (2004), "Large eddy simulation using an unstructured mesh based finite-volume solver", *34th AIAA*

- Fluid Dynamics Conf. and Exhibit*, Portland, Oregon.
- Kim, W.W. and Menon, S. (1995), "A new dynamic one-equation subgrid-scale model for large eddy simulations", *AIAA, 33rd Aerospace Sciences Meeting and Exhibit*, Reno, NV.
- Launder, B.E. and Spalding, D.B. (1974), "The numerical computation of turbulent flows", *Comput. Methods Appl. M.*, **3**, 269-289.
- Letchford, C.W., Iverson, R.E. and McDonald, J.R. (1993), "The application of the quasi-steady theory to full scale measurements on the Texas Tech Building", *J. Wind Eng. Ind. Aerod.*, **48**, 111-132.
- Li, Q.S., Calderone, I. and Melbourne, W.H. (1999), "Probabilistic characteristics of pressure fluctuations in separated and reattaching flows for various free-stream turbulence", *J. Wind Eng. Ind. Aerod.*, **82**(1-3), 125-145.
- Li, Q.S. and Melbourne, W.H. (1999), "The effects of large scale turbulence on pressure fluctuations in separated and reattaching flow", *J. Wind Eng. Ind. Aerod.*, **83**, 159-169.
- Li, Q.S., Fang, J.Q., Jeary, A.P., Wong, C.K. and Liu, D.K. (2000), "Evaluation of wind effects on a super tall building based on full scale measurements", *Earthq. Eng. Struct. D.*, **29**(12), 1845-1862.
- Li, Q.S., Yang, K., Wong, C.K. and Jeary, A.P. (2003), "The effect of amplitude-dependent damping on wind induced vibrations of a super tall building", *J. Wind Eng. Ind. Aerod.*, **91**, 1175-1198.
- Li, Q.S., Xiao, Y.Q., Wong, C.K. and Jeary, A.P. (2004), "Field measurements of typhoon effects on a super tall building", *Eng. Struct.*, **26**, 233-244.
- Lilly, D.K. (1992), "A proposed modification of the Germano subgrid-scale closure method", *Phys. Fluids*, **4**(3), 633-635.
- Mochida, A., Tominaga, Y., Murakami, S., Yoshie, R., Ishihara, T. and Ooka, R. (2002), "Comparison of various k-epsilon models and DSM applied to flow around a high-rise building - report on AIJ cooperative project for CFD prediction of wind environment", *Wind Struct.*, **5**(2-4), 227-244.
- Murakami, S. (1998), "Overview of turbulence models applied in CWE-1997", *J. Wind Eng. Ind. Aerod.*, **74-76**, 1-24.
- National Standard of the People's Republic of China (2001), *Chinese code for loading on buildings and structures*, GB50009-2001.
- Richards, P.J. and Hoxey, R.P. (2006), "Flow reattachment on the roof of a 6 m cube", *J. Wind Eng. Ind. Aerod.*, **94**(2), 77-99.
- Robertson, A.P., Hoxey, R.P., Rideout, N.M. and Freathy, P. (2007), "Full-scale study of wind loads on roof tiles and felt underlay and comparisons with design data", *Wind Struct.*, **10**(6), 495-510.
- Smagorinsky, J. (1963), "General circulation experiments with the primitive equations. I. the basic experiment", *Mon. Weather Rev.*, 99-164.
- Tutar, M. and Celik, I. (2007), "Large eddy simulation of a square cylinder flow: Modelling of inflow turbulence", *Wind Struct.*, **10**(6), 511-532.
- Uematsu, Y. and Isyumov, N. (1998), "Peak gust pressures acting on the roof and wall edges of a low-rise building", *J. Wind Eng. Ind. Aerod.*, **77-78**, 217-231.
- Welch, P. (1967), "The use of fast Fourier transform for the estimation of power spectra: A method based on time averaging over short", *IEEE T. Audio Electro.*, modified periodograms, **15**(2), 70-73.
- Wilcox, D.C. (1993), *Turbulence modeling for CFD*, La Canada, CA, DCW Industries, Inc.
- Zhang, N., Jiang, W.M. and Miao, S.G. (2006), "A large eddy simulation on the effect of buildings on urban flows", *Wind Struct.*, **9**(1), 23-35.